Precision Medicine and Imaging

Clinical Cancer Research

Distinguishing Tumor from Associated Fibrosis to Increase Diagnostic Biopsy Yield with Polarization-Sensitive Optical Coherence Tomography

Lida P. Hariri[1,2,3,4], David C. Adams[1,3,4], Matthew B. Applegate[1,3], Alyssa J. Miller[1,3], Benjamin W. Roop[1,3], Martin Villiger[3,4], Brett E. Bouma[3,4], and Melissa J. Suter[1,3,4]

Abstract

Purpose: With recent advancements in personalized medicine, biopsies must contain sufficient tumor for histologic diagnosis and molecular testing. However, inadvertent biopsy of tumor-associated fibrosis compromises tumor yield, resulting in delayed diagnoses and/or repeat procedures when additional tumor is needed. The ability to differentiate tumor from fibrosis intraprocedurally during biopsy could significantly increase tumor yield. Polarization-sensitive optical coherence tomography (PS-OCT) is an imaging modality that is endoscope- and/or needle-compatible, and provides large volumetric views of tissue microstructure with high resolution (~10 μm) while simultaneously measuring birefringence of organized tissues such as collagen. We aim to determine whether PS-OCT can accurately detect and distinguish tumor-associated fibrosis from tumor.

Experimental Design: PS-OCT was obtained *ex vivo* in 64 lung nodule samples. PS-OCT birefringence was measured and correlated to collagen content in precisely matched histology, quantified on picrosirius red (PSR) staining.

Results: There was a strong positive correlation between PS-OCT measurement of birefringent fibrosis and total collagen content by PSR ($r = 0.793$; $P < 0.001$). In addition, PS-OCT was able to accurately classify tumor regions with >20% fibrosis from those with low fibrosis ($\leq$20%) that would likely yield higher tumor content ($P < 0.0001$).

Conclusions: PS-OCT enables accurate fibrosis detection and can distinguish tumor regions with low fibrosis. PS-OCT has significant potential for clinical impact, as the ability to differentiate tumor from fibrosis could be used to guide intraprocedural tissue sampling *in vivo*, or for rapid biopsy adequacy assessment *ex vivo*, to increase diagnostic tumor yield essential for patient care and research.

Introduction

Tissue biopsy is the principal method used to diagnose tumors in a variety of organ systems. It is essential to maximize tumor yield in biopsy specimens for both clinical and research purposes. This is especially imperative in clinical scenarios requiring chemotherapy and/or radiotherapy, neoadjuvant or otherwise, where biopsy is the sole source of tumor tissue from a patient. This is also of significant importance in tumors where adequate tissue is needed for: (i) diagnosis, requiring hematoxylin and eosin (H&E) and possibly IHC stains for accurate tumor subtyping, and (ii) molecular testing to identify patients who may benefit from mutation-specific targeted therapy, such as in lung adenocarcinomas (1–6). Most carcinomas contain a mixture of tumor and other nontumor elements, such as stromal fibrosis, which is seen prominently in lung, breast, and pancreatic carcinomas. Inadvertent sampling of fibrotic tissue contaminates biopsies, decreases tumor yield, and can even impede diagnosis (5–7). Correspondingly, tumor collection for research purposes, such as biobanking and establishment of patient-derived primary tumor cell lines, are more likely to be successful when samples contain maximal tumor tissue (8). Fibrotic stroma is a known, challenging contaminant in research specimens. This contamination is vexing due to the abundant resources used to procure and store these sample collections and the reliance on ample tumor cell collection for execution of successful research studies.

Because of significant advancements in personalized medicine in lung carcinomas, there have been major efforts to maximize tumor yield in lung nodule biopsy (1–6). Guidance techniques, such as endobronchial ultrasound (EBUS), electromagnetic navigation (EMN), and CT-guided transthoracic biopsy, have been developed to help guide biopsy tools to the location of a targeted nodule to improve yield (2, 3, 9–11). However, these techniques do not provide insight into tumor composition, and therefore, cannot distinguish regions of tumor from admixed contaminant

[1]Division of Pulmonary and Critical Care Medicine, Massachusetts General Hospital, Boston, Massachusetts. [2]Department of Pathology, Massachusetts General Hospital, Boston, Massachusetts. [3]Wellman Center for Photomedicine, Massachusetts General Hospital, Boston, Massachusetts. [4]Harvard Medical School, Boston, Massachusetts.

Note: Supplementary data for this article are available at Clinical Cancer Research Online (http://clincancerres.aacrjournals.org/).

Corresponding Authors: Lida P. Hariri, Harvard Medical School, 55 Fruit St., Warren Building, Room 407, Boston, MA 02114. Phone: 617-726-6566; Fax: 617-726-4103; E-mail: lhariri@mgh.harvard.edu; and Melissa J. Suter, Harvard Medical School, 55 Fruit St., Warren Building, Room 407, Boston, MA 02114. Phone: 617-724-7691; Fax: 617-726-4103; E-mail: msuter@partners.org

Clin Cancer Res 2019;25:5242–9

doi: 10.1158/1078-0432.CCR-19-0566

Translational Relevance

Biopsy samples must have sufficient tumor for all required histologic and molecular diagnostic testing, particularly in lung carcinomas. However, contamination from tumor-associated fibrosis can yield inadequate biopsies and necessitate repeat procedures. Research biobanking also suffers from fibrosis contamination reducing tumor yields. The ability to detect and distinguish fibrosis from tumor at the time of collection could significantly improve tumor yield in all these settings. In this study, we demonstrated that polarization-sensitive OCT (PS-OCT) can accurately identify and distinguish tumor-associated fibrosis from tumor using birefringence detection. Our results demonstrate a strong correlation between PS-OCT and matched histology for fibrosis quantification. We demonstrate that PS-OCT can reliably distinguish tumor regions with low fibrosis ($\leq$20%) from those with >20% fibrosis. PS-OCT has significant potential for impact by increasing tumor yield for clinical and research purposes, either *in vivo* via needle-based imaging for biopsy guidance and/or *ex vivo* for rapid biopsy adequacy assessments.

fibrotic stroma. Rapid on-site evaluation (ROSE) of fine-needle aspiration (FNA) cytology has been implemented to improve yields in lung nodule biopsy, which has been effective but has limitations. ROSE is a retrospective assessment of collected FNA tissues, and as a result, is susceptible to false negative reads due to biopsy sampling error. ROSE cannot reliably quantify tumor amount on FNA, and rapid assessment of core biopsy tumor content is problematic due to consumption of tumor during frozen section assessment or touch prep (12). When there is inadequate tumor on initial biopsy, patients often must undergo repeat biopsy or more invasive procedures, such as video-assisted thoracoscopic surgical (VATS) wedge resection, to obtain additional material.

There is a clear need to optimize tumor yield and minimize contaminant fibrosis in biopsy specimens. Optical coherence tomography (OCT) is a nondestructive optical imaging modality that provides rapid, large volume, depth-resolved (~1–2 mm penetration depth depending on tissue scatter properties), high-resolution (<10 μm) images of tissue microstructure (13, 14). OCT has been successfully applied to disease detection in many organ systems, including the cardiovascular, gastrointestinal, ocular, and pulmonary systems (15–25). OCT imaging can be employed for either *in vivo* or *ex vivo* microarchitectural tissue assessment. In the pulmonary tract, both endobronchial and needle-based OCT catheters, compatible with standard bronchoscopy and transbronchial needles, have been developed that could be used for rapid, intraprocedural imaging of tissues surrounding the needle immediately prior to sample collection (26–28). Benchtop OCT systems can also be readily used for rapid *ex vivo* assessment of collected tissue specimens, including biopsy samples and resection specimens (29).

OCT has been shown capable of assessing and distinguishing lung parenchyma from pulmonary nodules with > 90% sensitivity and specificity, which has potential to improve diagnostic yield by providing microscopic guidance for needle biopsy as a complement to macroscopic guidance techniques such as EBUS and EMN (23, 24). However, the ability to distinguish tumor from admixed nondiagnostic fibrosis is crucial to the utility of OCT in guiding biopsy site selection and increasing tumor yield (25). Linearly organized tissues, such as collagen in fibrosis, demonstrate birefringence signatures (30, 31). Polarization-sensitive OCT (PS-OCT) is a modification to traditional OCT that detects tissue birefringence while simultaneously generating structural OCT images, and therefore, provides a means to detect fibrosis (31–35). Many groups, including ours, have shown that PS-OCT has potential to distinguish birefringent fibrosis from other tissue types, including tumors of the skin, larynx, breast, and lung (25, 36–42), but the majority of these studies have been qualitative in nature. Nadkarni and colleagues demonstrated that PS-OCT can be used to accurately quantify collagen in coronary atherosclerotic plaques to assist in intracoronary plaque assessment (31). Similar quantitative validation studies are foundational to assessing the true clinical potential of PS-OCT in tumor assessment and biopsy guidance. In this study, we investigate the ability of PS-OCT to quantify fibrotic stroma and distinguish low versus high fibrosis content in primary lung tumors.

Materials and Methods

Benchtop PS-OCT imaging was performed in a total of 64 tumor samples from fresh *ex vivo* lung resection specimens obtained from 26 patients. The Partners Healthcare Institutional Review Board (IRB) approved this study (protocol number: 2010-P-002214/1). Studies were conducted in accordance with the Ethical Principles and Guidelines for the Protection of Human Subjects of Research, known as the Belmont Report. The informed written consent process was waived due to the use of deidentified excess tissue in this study, as approved by the Partners IRB. To ensure accurate registration with histology, regions of interest were demarcated in tissue samples using two needle marks (26-gauge) and tissue marking dye (Triangle Biomedical Sciences) visible in both PS-OCT imaging and histology. For each PS-OCT and histology pair, the region of interest was precisely registered on the basis of the location of the inked needle marks. The details of the ink mark registration procedure have previously been described in detail (43).

PS-OCT imaging, processing, and birefringence calculation

The technical details of the PS-OCT system and methods used in this study to generate PS-OCT images have been previously described in detail (14, 22, 32–35, 44–46). Briefly, we used a custom-built fiber-based swept-source OCT system with a center wavelength of 1,310 nm, a bandwidth of 110 nm, and an A-line acquisition rate of 66 kHz. A benchtop microscope, with a telecentric lens with a spot size approximately 20 μm, was used to image the tissue samples. The axial resolution of the OCT system was approximately 7 μm in tissue. Lateral and transverse scanning were achieved using galvonometric mirrors.

Conventional structural OCT and PS-OCT images were obtained simultaneously, and images were generated from the raw datasets offline. Structural OCT images were processed and displayed by use of an inverse gray-scale lookup table. Polarization sensitivity was achieved by modulating the polarization state of the source between perpendicular polarization states in successive axial depth profiles (A-lines), then combining A-line pairs by Stokes vector analysis (22, 32–35, 46). PS-OCT images were processed using a spectral binning method to mitigate polarization mode dispersion, which has previously been described in

detail (46). Differential (local) retardation was calculated from spectrally binned data using a depth offset of approximately 24 μm (in tissue).

Out-of-frame averaging was performed on OCT images over 30 frames, or approximately 60 μm, to reduce speckle noise. Structural OCT images were thresholded to remove signal < 30 dB to remove noise. PS-OCT birefringence was thresholded to remove signal < 20 degrees/100 μm, based on birefringence values from previously published data (22). The thresholded structural image was then used to mask the corresponding thresholded PS-OCT image to isolate birefringence signal arising from tissue. The PS-OCT region of interest (ROI) was defined as the distance between the two registration ink marks (range 2.6–8.8 mm) by 0.25 mm depth. The depth of 0.25 mm was chosen to mitigate signal roll off within tissue. The percent fibrosis in the PS-OCT ROI was calculated as the number of pixels with birefringence measurements $\geq$ 20 degrees/100 μm divided by the total number of pixels in the ROI. All data processing was performed using Matlab.

Histologic analysis of fibrosis

Following imaging, the tissue specimens were fixed in 10% formalin and processed using standard histology techniques. Tissue sections (5-μm thick) were cut cross-sectionally, traversing the registration ink marks. Sequential sections were stained with hematoxylin and eosin (H&E) or picrosirius red (PSR), a stain for collagen (47, 48). Collagen content was measured within the PSR ROI morphometrically using digitized images of the PSR-stained sections, obtained with a circularly polarized light microscope (Olympus BX43, Olympus America). The camera exposure time was set to prevent saturation and was kept constant for all cases at 60 ms, with zero gain. The PSR ROI was defined as the distance measured laterally between the ink marks (x-axis) by 0.25 mm in depth (y-axis) on one PSR slide, corresponding to the PS-OCT ROI. Collagen fibers in PSR visualized under polarized light microscopy appear as either orange-red or yellow-green, depending on fiber thickness. Collagen fibers were identified in PSR images based on the corresponding hue values, after a saturation threshold of $\leq$ 25 was applied to remove noise. Total collagen content was computed by dividing the number of pixels corresponding to collagen fibers (hue values in red/orange: 1-38, 230-256, or yellow-green: 39-128) by the total number of pixels in the ROI. This method has been previously described in detail (31, 47, 48).

Statistical analysis

Linear regression analysis was performed to test the correlation between PS-OCT birefringence imaging and histologic PSR collagen measurements in matched ROIs. Fisher exact test was performed to determine the ability of PS-OCT to distinguish tumor regions with low fibrosis content ($\leq$20%) from tumor regions with > 20% fibrosis. A 20% cutoff was chosen to determine whether PS-OCT could accurately identify tumor-rich regions likely to yield high tumor sampling. Bland–Altman analysis was performed to compare the amount of measured collagen for the two measuring techniques. The difference was calculated as the percent collagen measured by PSR minus the percent collagen detected by PS-OCT in matched ROIs. For all analyses, a P value of < 0.05 was considered statistically significant. All statistical analyses were performed using GraphPad.

Results

Histology

PS-OCT was obtained from 64 tumor samples [31 adenocarcinomas, 30 squamous cell carcinomas (SCC), 2 carcinoid tumors, 1 hamartoma] from *ex vivo* lung resection specimens from 26 patients. Of these, 7 samples from 3 patients were removed from the analysis due to issues with ink marks prohibiting accurate PS-OCT:histology matching (n = 3), or technical issues with PS-OCT data acquisition (n = 4). The remaining 57 samples from 23 patients were included in the testing dataset (Table 1).

PS-OCT fibrosis detection

Total collagen content measured morphometrically from PSR-stained sections under polarized light microscopy ranged from 0.2 to 83.9% among the tumor samples. Linear regression analysis showed a strong positive correlation in total collagen detected in PS-OCT birefringence imaging and total collagen content measured by PSR (r = 0.793, P <0.001), as demonstrated in Fig. 1. Fisher exact test demonstrated that PS-OCT was able to classify tumor regions with low fibrosis content ($\leq$20%) from those with >20% fibrosis (P <0.0001), as demonstrated in Table 2. The sensitivity and specificity of PS-OCT for low fibrosis tumor regions ($\leq$20%) was 0.95 and 0.80, respectively. The overall classification accuracy was 0.91. Bland–Altman analysis demonstrated an average bias of 3.898%, indicating that PSR measures more collagen than does PS-OCT. Bland–Altman analysis on the low fibrosis group ($\leq$20% fibrosis) demonstrated a bias of −0.338% (Fig. 2), indicating that PS-OCT fibrosis detection is more accurate when there is low fibrosis content. Additional Fisher exact test analyses with threshold cutoffs for low fibrosis set at $\leq$18.5% and $\leq$22.5% were also performed (Supplementary Tables S1 and S2), which yielded similar results (P < 0.0001 for both threshold values).

In addition to fibrosis quantification, PS-OCT also provides information about the microscopic distribution of fibrosis and tumor within lung nodules. Figure 3A and B shows an illustrative PS-OCT image of a squamous cell carcinoma (SCC) with regional dense fibrosis. In the right half of the ROI, there is dense birefringent collagen visualized with PS-OCT, and confirmed by PSR staining, indicating the right side is not an ideal site for biopsy. However, the left side of the image contains little birefringent fibrosis, which indicates that this region is likely to yield more tumor in a biopsy sample. Figure 3C and D shows an illustrative

Table 1. Clinical characteristics

Age	71 years (range, 57–84 years)
Sex	14 F/9 M
Diagnosis	
Adenocarcinoma	30 samples (14 patients)
SCC	24 samples (6 patients)
Carcinoid	2 samples (2 patients)
Hamartoma	1 sample (1 patient)
Size of lesion	3.1 mm (range, 1.2–6.3 mm)
Stage	
pT1a	4 patients
pT1b	5 patients
pT2a	7 patients
pT2b	2 patients
pT3	4 patients
N status	
Nx	3 patients
N0	17 patients
N1	1 patient
N2	1 patient

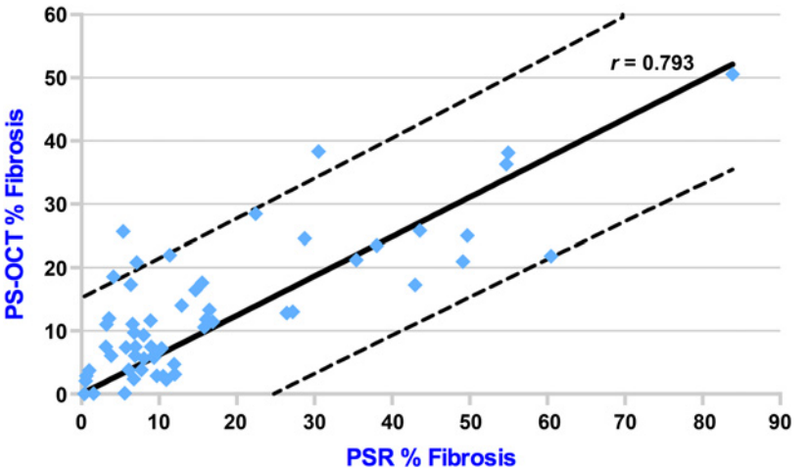

Figure 1.
Relationship between fibrosis detection in PS-OCT and PSR staining. A high positive correlation ($r = 0.793$) is demonstrated between PS-OCT and PSR for quantifying percent fibrosis within the ROI. The dotted lines show 95% prediction intervals.

PS-OCT image of an adenocarcinoma with focal fibrosis, occupying approximately 25% of the total ROI, which could be avoided during biopsy sampling. Corresponding PSR staining confirms the focus of fibrosis within the adenocarcinoma in the same ROI region. These two cases illustrate the ability of PS-OCT to detect contaminant fibrosis and provide microscopic spatial mapping of the tumor/fibrosis distribution within a nodule. This would be useful in guiding biopsy-site sampling locations *in vivo* and tumor collection sites for molecular testing and/or biobanking *ex vivo*.

Figure 4A and B illustrate a noninvasive lepidic adenocarcinoma, with minimal fibrosis present within the alveolar walls throughout the ROI on PSR staining that is typical of this adenocarcinoma subtype histologically. The corresponding PS-OCT image demonstrates minimal interstitial birefringence throughout the ROI. Figure 4C and D shows an illustrative example of an SCC with solid morphology. Essentially, no birefringent collagen was seen on PS-OCT imaging or PSR staining. These two cases illustrate the ability of PS-OCT to detect tumor regions with little to no contaminant fibrosis, indicating adequate biopsy-site locations, as well as potential to provide some microarchitectural insights into morphologic patterns. Supplementary Figures S1–S5 present additional examples of PS-OCT and PSR-matched pairs from the dataset.

Discussion

Biopsy samples must have adequate tumor yields to satisfy both histologic and molecular diagnostics, particularly in lung carcinomas. However, when inadequate tumor sampling occurs, it is often in large part from inadvertent biopsy of tumor-associated fibrosis within the lesion. In this study, we demonstrated that PS-OCT can accurately identify tumor-associated fibrosis, and distinguish it from tumor, using tissue birefringence detection. Our results demonstrate a strong correlation between PS-OCT birefringence and PSR histology measurement of fibrosis content. This validation study is an essential step in the clinical translation of the technology, which has significant potential for impact to increase tumor yield in a variety of clinical and research settings.

Physicians performing lung biopsies seek to obtain the highest possible tumor yield in the sample for current and potential future individual patient care needs, as well as potential banking/research purposes (5, 6). In a study examining the compositions of samples containing ≤ 30% tumor, 87.1% of the samples contained some amount of fibrosis, and 41.6% had fibrosis as their most abundant nontumor component (7). PS-OCT could be implemented *in vivo* for intraprocedural biopsy guidance to avoid contaminant fibrosis and increase tumor yield. Needle-based OCT probes have been developed that are compatible with bronchoscopy and TBNA, which would allow PS-OCT imaging of tissues around the needle prior to sample collection (26–28). We have previously shown that structural OCT is capable of distinguishing lung nodules and lung parenchyma with high sensitivity and specificity (>90%) and can be utilized to ensure

Table 2. Fisher exact contingency table: classifying tumor regions by fibrotic content with PS-OCT versus PSR

	PS-OCT		
	≤20%	>20%	Total
PSR			
≤20%	40	2	42
>20%	3	12	15
Total	43	14	57

NOTE: Fisher exact test–demonstrated PS-OCT accurately classified tumor regions with low fibrosis content (≤20%) from those with >20% fibrosis ($P < 0.0001$), with few false positive and negative cases. The sensitivity and specificity of PS-OCT for low fibrosis tumor regions (≤20%) was 0.95 and 0.80, respectively. The overall classification accuracy was 0.91.

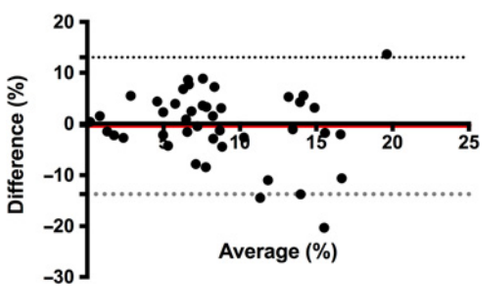

Figure 2.
Bland–Altman plot for low fibrosis cases. The dotted lines indicate the upper and lower 95% confidence intervals, and the red line indicates the bias. In the analysis of the low fibrosis (≤20% fibrosis) cases, there is minimal bias of −0.338%.

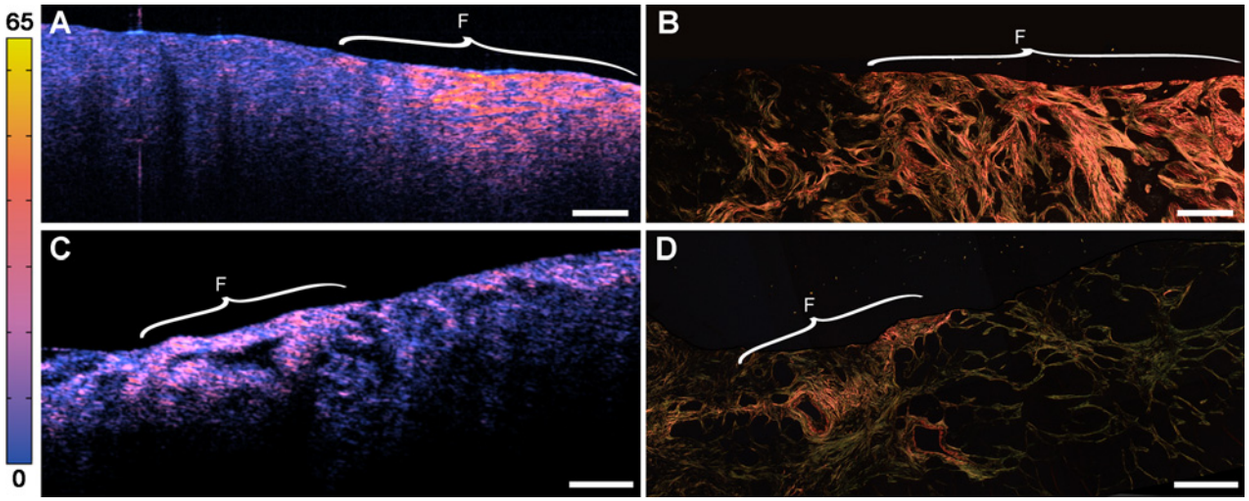

Figure 3.

PS-OCT and PSR images of lung carcinomas with fibrosis. **A,** PS-OCT image of a squamous cell carcinoma (SCC) with dense birefringent fibrosis (F) on the right, confirmed by corresponding PSR staining (**B**, F). The left side of the image contains little birefringent fibrosis, indicating this region is likely to yield higher tumor content in a biopsy sample. **C,** PS-OCT image of an adenocarcinoma with focal birefringent fibrosis (F), with corresponding PSR staining (**D**) confirming the focus of fibrosis (F) in the same ROI region. PS-OCT detects fibrosis and provides microscopic mapping of tumor/fibrosis distribution within a nodule, which would be useful in guiding biopsy sampling locations. Scale bars, 0.5 mm. PS-OCT images (**A** and **C**) display the measured birefringence overlaid on the corresponding structural OCT image. Birefringence map on left indicates amount of birefringence in PS-OCT in degrees/100 μm (range, 0–65 degrees/100 μm).

accurate targeting of a nodule (23). The additional ability to distinguish tumor from adjacent fibrosis within the nodule has significant potential to increase tumor yield and reduce the need for repeat and/or more invasive procedures to acquire more tumor tissue.

In this study, we found that PS-OCT fibrosis detection was strongly correlated to PSR histology measurement of fibrosis content. Bland–Altman analysis revealed there was small bias such that overall, PSR detected more collagen than PS-OCT. However, within the low fibrosis group, the average difference

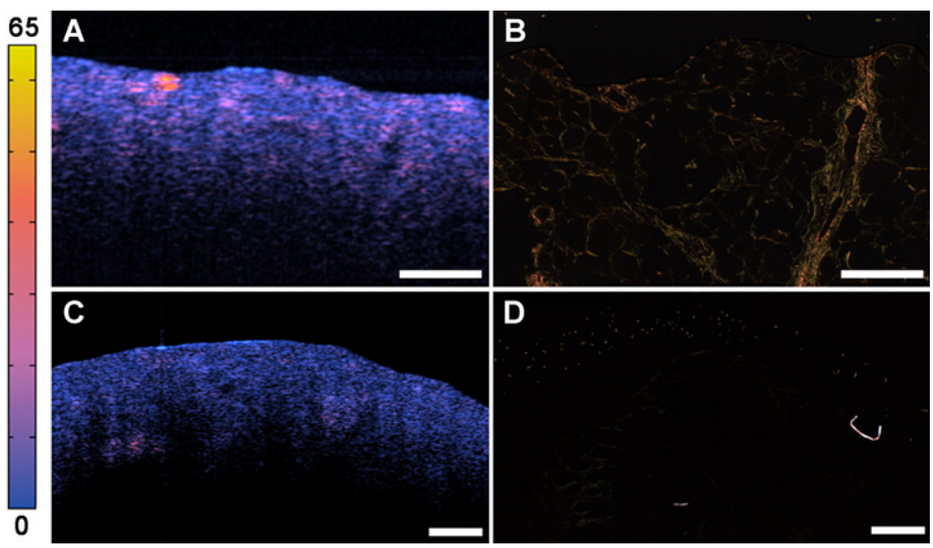

Figure 4.

PS-OCT and PSR images of lung carcinomas with minimal to no fibrosis. **A,** PS-OCT image of a noninvasive lepidic adenocarcinoma, with minimal interstitial birefringent fibrosis present throughout the ROI. **B,** PSR staining confirms minimal fibrosis within alveolar walls, which is typical of lepidic adenocarcinoma pattern histologically. **C,** PS-OCT image of a squamous cell carcinoma with solid morphology. Essentially, no birefringent collagen was seen on PS-OCT imaging, confirmed by PSR staining (**D**). PS-OCT detects tumor regions with little to no contaminant fibrosis, indicating adequate biopsy-site locations, and can also provide some microarchitectural insights into the morphologic patterns of the carcinoma. Scale bars, 0.5 mm. PS-OCT images (**A** and **C**) display the measured birefringence overlaid on the corresponding structural OCT image. Birefringence map on left indicates amount of birefringence in PS-OCT in degrees/100 μm (range, 0–65 degrees/100 μm).

between measurements was negligible (−0.338%), suggesting that both methods produce nearly identical results when measuring in low fibrosis content regions.

The results of our study are an essential step toward translating PS-OCT to the *in vivo* biopsy guidance setting. However, our findings must be validated in large-scale clinical studies. PS-OCT could also be implemented for *ex vivo* tissue assessment using benchtop imaging stations. Potential *ex vivo* applications include using PS-OCT for rapid adequacy assessment of biopsy specimens without consuming, freezing, or damaging tissue, or for selection of tissue for clinical purposes, biobanking, primary cell culture, or other research purposes, from either biopsy or whole lung resection specimens.

In addition to quantifying fibrosis, PS-OCT also provides the ability to visualize fibrosis distribution, which adds further benefit for guiding tumor sampling sites *in vivo* and *ex vivo*. This is exemplified in the illustrative cases in Figs. 3 and 4. In Fig. 3A and B, although the quantified fibrosis burden was high, PS-OCT revealed that dense fibrosis occupied predominantly the right half of the ROI. Tumor collection from the left half of the ROI would likely yield a successful sample. In Fig. 3C and D, PS-OCT revealed that the majority of the ROI contained tumor, with only a focal region abundant in fibrosis that could be avoided during tumor biopsy/collection. PS-OCT also has the potential to inform on the underlying pattern of the carcinoma. In Fig. 4A and B, PS-OCT demonstrated minimal interstitial fibrosis present throughout the ROI, reflecting the minimal alveolar wall fibrosis of lepidic adenocarcinoma and indicating that the entire ROI would be adequate for tumor biopsy/collection. In contrast, Fig. 4C and D revealed a solid pattern of carcinoma with essentially no fibrosis within the ROI, providing information both on the suitability of the biopsy site as well as potential insights in to the tumor pattern present in the ROI.

For successful translation to clinical use, the data processing and analysis must be achievable within clinically acceptable timeframes. In this study, we used Matlab for PS-OCT image processing, which currently takes approximately 2 seconds/frame. The use of a more efficient programming language would significantly speed up image processing times so that processing could be performed in real time. The PS-OCT fibrosis quantification process described in this study was nearly fully automated, with processing rates of approximately 30 frames/second. This was also performed using Matlab, and could be sped up with another programming language if necessary. The only portion of the quantification algorithm that was performed manually was defining the lateral aspect (*x*-axis) of the ROI. This was not automated in this study because the lateral ROI distance was different for each sample (defined by the distance between the ink registration marks) to compare against the matched PSR ROI. In the clinical setting, a simple tissue surface identification algorithm would be sufficient. Our laboratory has already published automated methods for tissue surface identification, which could easily be applied to this setting (22, 49).

This study focused on assessment of primary lung tumors, due to the eminent clinical necessity to increase tumor yield to meet histologic and molecular testing needs in lung carcinomas. However, fibrosis contamination in biopsies is known to occur in many other primary malignancy sites, such as breast and pancreatic carcinoma. Collagen present within tumors at other primary sites is anticipated to have similar organizational arrangements as seen in lung primary malignancies. Therefore, it is expected that fibrosis within other primary tumor sites would exhibit similar birefringence detectable by PS-OCT. Therefore, the ability to quantify fibrosis burden is likely to be translatable to other organ sites. Other groups have conducted pilot studies investigating PS-OCT for fibrosis detection in breast carcinoma (36–38) and the results of our study concur with their findings. However, follow-up studies are needed to confirm the translatability of our findings in other primary tumor sites. Fibrosis detection by PS-OCT also has potential to make significant clinical impacts in non-neoplastic disease entities such as fibrotic interstitial lung diseases including usual interstitial pneumonitis (21), airway changes in asthma (22), and skin fibrosis in systemic sclerosis.

Our data showed some trends where PS-OCT seemed to overestimate at low collagen levels and underestimate at high collagen levels. Samples with low collagen levels are more likely to contain younger, less organized, and/or less dense collagen, which will have lower birefringence signals that may be near the noise floor. It is possible that minor modifications to the noise floor threshold may assist in increasing the fibrosis detection accuracy in these cases. Although the PSR stain is the standard histologic stain for collagen detection, it has been described in the literature that PSR is an imperfect method for collagen quantification (50, 51). It is possible that PSR underestimated collagen in the low fibrosis cases. Samples with high fibrosis levels may contain storiform patterns of dense collagen, which may include small regions where the fibers are oriented parallel to the incident OCT beam (see Supplementary Fig. S5). When collagen is oriented parallel to the beam, birefringence will not be detected and therefore, total collagen content will be underestimated. Registration between PS-OCT images and histology sections were performed by using ink marks to define the ROI, applied to the tissue using a 26-gauge needle. Therefore, the precision of the registration between PS-OCT and histology was approximately 500 μm. Patterns of fibrosis are known to vary within tumor nodules, and lack of exact precision in PS-OCT and corresponding PSR matches may have led to differences in the amount of fibrosis measured by each modality. Despite these limitations, the correlation between PS-OCT and PSR fibrosis detection was high.

In this study, we demonstrate that PS-OCT detection of birefringent collagen allows for accurate distinction of fibrosis and tumor within tumor nodules, which is an essential step in translating the technology for clinical use to increase tumor yield in biopsy specimens. We assessed PS-OCT imaging in *ex vivo* lung tumor nodules and compared fibrosis detection against corresponding histology stained with PSR, demonstrating high correlation between the two modalities. PS-OCT was able to reliably identify tumor regions with low fibrosis content ($\leq$20%). We anticipate that these findings will have significant potential for clinical applications, through *in vivo* needle-based PS-OCT imaging performed intraprocedurally to guide biopsy-site selection and/or *ex vivo* benchtop PS-OCT imaging for rapid biopsy adequacy assessment or selection of biobanking/research tissues.

Disclosure of Potential Conflicts of Interest

L.P. Hariri is a consultant/advisory board member for LX Medical. B.E. Bouma holds ownership interest (including patents) in NinePoint Medical. M.J. Suter is a consultant for LX Medical and NinePoint medical, and is listed as a co-inventor on a number of patents and patent applications related to Optical Coherence Tomography Imaging, owned by Massachusetts General Hospital. No potential conflicts of interest were disclosed by the other authors.

Authors' Contributions

Conception and design: L.P. Hariri, M.J. Suter
Development of methodology: L.P. Hariri, M. Villiger, B.E. Bouma, M.J. Suter
Acquisition of data (provided animals, acquired and managed patients, provided facilities, etc.): L.P. Hariri, M.B. Applegate, A.J. Miller, M. Villiger, B.E. Bouma, M.J. Suter
Analysis and interpretation of data (e.g., statistical analysis, biostatistics, computational analysis): L.P. Hariri, D.C. Adams, B.W. Roop, M.J. Suter
Writing, review, and/or revision of the manuscript: L.P. Hariri, D.C. Adams, M.B. Applegate, A.J. Miller, B.W. Roop, M. Villiger, B.E. Bouma, M.J. Suter
Administrative, technical, or material support (i.e., reporting or organizing data, constructing databases): L.P. Hariri, M.B. Applegate, A.J. Miller, B.W. Roop
Study supervision: L.P. Hariri, M.J. Suter

Acknowledgments

This work was funded in part by the NIH (grant numbers R01CA167827, K23HL132120, T32CA009216), a grant from the LUNGevity Foundation/Upstage Lung Cancer (grant number 2016-02), and a grant from the American Lung Association (RT-342501).

The costs of publication of this article were defrayed in part by the payment of page charges. This article must therefore be hereby marked *advertisement* in accordance with 18 U.S.C. Section 1734 solely to indicate this fact.

Received February 21, 2019; revised April 9, 2019; accepted June 3, 2019; published first June 7, 2019.

References

1. Travis WD, Brambilla E, Noguchi M, Nicholson AG, Geisinger KR, Yatabe Y, et al. International Association for the Study of Lung Cancer/American Thoracic Society/European Respiratory Society international multidisciplinary classification of lung adenocarcinoma. J Thorac Oncol 2011;6:244–85.
2. Rivera MP, Mehta AC. Initial diagnosis of lung cancer: ACCP evidence-based clinical practice guidelines (2nd edition). Chest 2007;132:131s–48s.
3. Wang Memoli JS, Nietert PJ, Silvestri GA. Meta-analysis of guided bronchoscopy for the evaluation of the pulmonary nodule. Chest 2011;142:385–93.
4. Simon GR, Silvestri GA. You just can't call it lung cancer anymore. J Thorac Oncol 2011;6:239–40.
5. Kerr KM. Personalized medicine for lung cancer: new challenges for pathology. Histopathology 2012;60:531–46.
6. Coghlin CL, Smith LJ, Bakar S, Stewart KN, Devereux GS, Nicolson MC, et al. Quantitative analysis of tumor in bronchial biopsy specimens. J Thoracic Oncol 2010;5:448–52.
7. Goh F, Duhig EE, Clarke BE, McCaul E, Passmore L, Courtney D, et al. Low tumour cell content in a lung tumour bank: implications for molecular characterisation. Pathology 2017;49:611–7.
8. Massett HA, Atkinson NL, Weber D, Myles R, Ryan C, Grady M, et al. Assessing the need for a standardized cancer HUman Biobank (caHUB): findings from a national survey with cancer researchers. J Natl Cancer Inst Monogr 2011;2011:8–15.
9. Mazzone P, Jain P, Arroliga AC, Matthay RA. Bronchoscopy and needle biopsy techniques for diagnosis and staging of lung cancer. Clin Chest Med 2002;23:137–58.
10. Shure D, Fedullo PF. Transbronchial needle aspiration of peripheral masses. Am Rev Respir Dis 1983;128:1090–2.
11. Dooms C, Seijo L, Gasparini S, Trisolini R, Ninane V, Tournoy KG. Diagnostic bronchoscopy: state of the art. Eur Respir Rev 2010;19:229–36.
12. da Cunha Santos G, Ko HM, Saieg MA, Geddie WR. "The petals and thorns" of ROSE (rapid on-site evaluation). Cancer Cytopathol 2013;121:4–8.
13. Huang D, Swanson EA, Lin CP, Schuman JS, Stinson WG, Chang W, et al. Optical coherence tomography. Science 1991;254:1178–81.
14. Yun SH, Tearney GJ, Vakoc BJ, Shishkov M, Oh WY, Desjardins AE, et al. Comprehensive volumetric optical microscopy in vivo. Nat Med 2006;12:1429–33.
15. Tearney GJ, Waxman S, Shishkov M, Vakoc BJ, Suter MJ, Freilich MI, et al. Three-dimensional coronary artery microscopy by intracoronary optical frequency domain imaging. JACC Cardiovasc Imaging 2008;1:752–61.
16. Suter MJ, Vakoc BJ, Yachimski PS, Shishkov M, Lauwers GY, Mino-Kenudson M, et al. Comprehensive microscopy of the esophagus in human patients with optical frequency domain imaging. Gastrointest Endoscopy 2008;68:745–53.
17. Hee MR, Izatt JA, Swanson EA, Huang D, Schuman JS, Lin CP, et al. Optical coherence tomography of the human retina. Arch Ophthalmol 1995;113:325–32.
18. Michel RG, Kinasewitz GT, Fung KM, Keddissi JI. Optical coherence tomography as an adjunct to flexible bronchoscopy in the diagnosis of lung cancer: a pilot study. Chest 2010;138:984–8.
19. Tsuboi M, Hayashi A, Ikeda N, Honda H, Kato Y, Ichinose S, et al. Optical coherence tomography in the diagnosis of bronchial lesions. Lung Cancer 2005;49:387–94.
20. Lam S, Standish B, Baldwin C, McWilliams A, leRiche J, Gazdar A, et al. In vivo optical coherence tomography imaging of preinvasive bronchial lesions. Clin Cancer Res 2008;14:2006–11.
21. Hariri LP, Adams DC, Wain JC, Lanuti M, Muniappan A, Sharma A, et al. Endobronchial optical coherence tomography for low-risk microscopic assessment and diagnosis of idiopathic pulmonary fibrosis in vivo. Am J Respir Crit Care Med 2018;197:949–52.
22. Adams DC, Hariri LP, Miller AJ, Wang Y, Cho JL, Villiger M, et al. Birefringence microscopy platform for assessing airway smooth muscle structure and function in vivo. Sci Transl Med 2016;8:359ra131.
23. Hariri LP, Mino-Kenudson M, Applegate MB, Mark EJ, Tearney GJ, Lanuti M, et al. Toward the guidance of transbronchial biopsy: identifying pulmonary nodules with optical coherence tomography. Chest 2013;144:1261–8.
24. Hariri LP, Applegate MB, Mino-Kenudson M, Mark EJ, Medoff BD, Luster AD, et al. Volumetric optical frequency domain imaging of pulmonary pathology with precise correlation to histopathology. Chest 2013;143:64–74.
25. Hariri LP, Villiger M, Applegate MB, Mino-Kenudson M, Mark EJ, Bouma BE, et al. Seeing beyond the bronchoscope to increase the diagnostic yield of bronchoscopic biopsy. Am J Respirat Crit Care Med 2013;187:125–9.
26. Tan KM, Shishkov M, Chee A, Applegate MB, Boume BE, Suter MJ. Flexible transbronchial optical frequency domain imaging smart needle for biopsy guidance. Biomed Optics Express 2012;3:1947–54.
27. Scolaro L, Lorenser D, McLaughlin RA, Quirk BC, Kirk RW, Sampson DD. High-sensitivity anastigmatic imaging needle for optical coherence tomography. Opt Lett 2012;37:5247–9.
28. Kuo WC, Kim J, Shemonski ND, Chaney EJ, Spillman DR Jr, Boppart SA. Real-time three-dimensional optical coherence tomography image-guided core-needle biopsy system. Biomed Opt Express 2012;3:1149–61.
29. Wells WA, Thrall M, Sorokina A, Fine J, Krishnamurthy S, Haroon A, et al. In vivo and ex vivo microscopy: moving toward the integration of optical imaging technologies into pathology practice. Arch Pathol Lab Med 2018;143:288–98.
30. Wolman M, Kasten FH. Polarized light microscopy in the study of the molecular structure of collagen and reticulin. Histochemistry 1986;85:41–9.
31. Nadkarni SK, Pierce MC, Park BH, de Boer JF, Whittaker P, Bouma BE, et al. Measurement of collagen and smooth muscle cell content in atherosclerotic plaques using polarization-sensitive optical coherence tomography. J Am Coll Cardiol 2007;49:1474–81.
32. de Boer JF, Milner TE. Review of polarization sensitive optical coherence tomography and Stokes vector determination. J Biomed Optics 2002;7:359–71.
33. Park BH, Pierce MC, Cense B, de Boer JF. Jones matrix analysis for a polarization-sensitive optical coherence tomography system using fiber-optic components. Opt Lett 2004;29:2512–4.
34. Oh WY, Vakoc BJ, Yun SH, Tearney GJ, Bouma BE. Single-detector polarization-sensitive optical frequency domain imaging using high-speed intra A-line polarization modulation. Opt Lett 2008;33:1330–2.

35. Oh WY, Yun SH, Vakoc BJ, Shishkov M, Desjardins AE, Park BH, et al. High-speed polarization sensitive optical frequency domain imaging with frequency multiplexing. Opt Express 2008;16:1096–103.
36. Villiger M, Lorenser D, McLaughlin RA, Quirk BC, Kirk RW, Bouma BE, et al. Deep tissue volume imaging of birefringence through fibre-optic needle probes for the delineation of breast tumour. Sci Rep 2016;6: 28771.
37. South FA, Chaney EJ, Marjanovic M, Adie SG, Boppart SA. Differentiation of ex vivo human breast tissue using polarization-sensitive optical coherence tomography. Biomed Opt Express 2014;5:3417–26.
38. Patel R, Khan A, Quinlan R, Yaroslavsky AN. Polarization-sensitive multimodal imaging for detecting breast cancer. Cancer Res 2014;74: 4685–93.
39. Burns JA, Kim KH, deBoer JF, Anderson RR, Zeitels SM. Polarization-sensitive optical coherence tomography imaging of benign and malignant laryngeal lesions: an in vivo study. Otolaryngol Head Neck Surg 2011;145: 91–9.
40. Mogensen M, Joergensen TM, Nurnberg BM, Morsy HA, Thomsen JB, Thrane L, et al. Assessment of optical coherence tomography imaging in the diagnosis of non-melanoma skin cancer and benign lesions versus normal skin: observer-blinded evaluation by dermatologists and pathologists. Dermatol Surg 2009;35:965–72.
41. Strasswimmer J, Pierce MC, Park BH, Neel V, de Boer JF. Polarization-sensitive optical coherence tomography of invasive basal cell carcinoma. J Biomed Opt 2004;9:292–8.
42. Kim KH, Burns JA, Bernstein JJ, Maguluri GN, Park BH, de Boer JF. In vivo 3D human vocal fold imaging with polarization sensitive optical coherence tomography and a MEMS scanning catheter. Optics Express 2010;18: 14644–53.
43. Hariri LP, Applegate MB, Mino-Kenudson M, Mark EJ, Bouma BE, Tearney GJ, et al. Optical frequency domain imaging of ex vivo pulmonary resection specimens: obtaining one to one image to histopathology correlation. J Vis Exp 2013. doi: 10.3791/3855.
44. Yun S, Tearney G, Bouma B, Park B, de Boer J. High-speed spectral-domain optical coherence tomography at 1.3 mum wavelength. Opt Express 2003; 11:3598–604.
45. Yun S, Tearney G, de Boer J, Bouma B. Removing the depth-degeneracy in optical frequency domain imaging with frequency shifting. Opt Express 2004;12:4822–8.
46. Villiger M, Zhang EZ, Nadkarni SK, Oh WY, Vakoc BJ, Bouma BE. Spectral binning for mitigation of polarization mode dispersion artifacts in catheter-based optical frequency domain imaging. Opt Express 2013;21: 16353–69.
47. Rich L, Whittaker P. Collagen and picrosirius red staining: a polarized light assessment of fibrillar hue and spatial distribution. 2005;22:97–104.
48. MacKenna DA, Omens JH, McCulloch AD, Covell JW. Contribution of collagen matrix to passive left ventricular mechanics in isolated rat hearts. Am J Physiol 1994;266:H1007–18.
49. Adams DC, Pahlevaninezhad H, Szabari MV, Cho JL, Hamilos DL, Kesimer M, et al. Automated segmentation and quantification of airway mucus with endobronchial optical coherence tomography. Biomed Opt Express 2017; 8:4729–41.
50. Lattouf R, Younes R, Lutomski D, Naaman N, Godeau G, Senni K, et al. Picrosirius red staining: a useful tool to appraise collagen networks in normal and pathological tissues. J Histochem Cytochem 2014;62:751–8.
51. Street JM, Souza ACP, AlvarezPrats A, Horino T, Hu X, Yuen PST, et al. Automated quantification of renal fibrosis with Sirius Red and polarization contrast microscopy. Physiol Rep 2014;2:e12088.